

How to Build the Optimal Magnet Assembly for Magnetocaloric Cooling: Structural Optimization with Isogeometric Analysis

Michael Wiesheu^a, Melina Merkel^a, Tim Sittig^b, Dimitri Benke^b, Max Fries^b, Sebastian Schöps^a, Oliver Weeger^c, Idoia Cortes Garcia^d

^aComputational Electromagnetics Group, Technical University of Darmstadt, Schloßgartenstr. 8, Darmstadt, 64289, Germany

^bMagnoTherm Solutions GmbH, Pfungstädter Str. 102, Darmstadt, 64297, Germany

^cCyber-Physical Simulation, Technical University of Darmstadt, Dolivostr. 15, Darmstadt, 64293, Germany

^dDepartment of Mechanical Engineering, Eindhoven University of Technology, Gemini-Zuid 0.143 PO Box 513, Eindhoven, 5600 MB, The Netherlands

Abstract

In the search for more efficient and less environmentally harmful cooling technologies, the field of magnetocalorics is considered a promising alternative. To generate cooling spans, rotating permanent magnet assemblies are used to cyclically magnetize and demagnetize magnetocaloric materials, which change their temperature under the application of a magnetic field. In this work, an axial rotary permanent magnet assembly, aimed for commercialization, is computationally designed using topology and shape optimization. This is efficiently facilitated in an isogeometric analysis framework, where harmonic mortaring is applied to couple the rotating rotor-stator system of the multipatch model. Inner, outer and co-rotating assemblies are compared and optimized designs for different magnet masses are determined. These simulations are used to homogenize the magnetic flux density in the magnetocaloric material. The resulting torque is analyzed for different geometric parameters. Additionally, the influence of anisotropy in the active magnetic regenerators is studied in order to guide the magnetic flux. Different examples are analyzed and classified to find an optimal magnet assembly for magnetocaloric cooling.

Keywords: Magnet Assembly, Magnetocalorics, Isogeometric Analysis, Shape Optimization, Topology Optimization, Harmonic Mortaring

1. Introduction

As of 2018, cooling contributed to 17 % of the worldwide electricity consumption and this demand is projected to triple by 2050 [1]. Furthermore, hydrofluorocarbons (HFCs) – highly potent greenhouse gases – are commonly used as refrigerants in conventional vapor-compression cooling systems. Combining direct emissions caused by the leakage of HFC refrigerant gases and indirect emissions from the power generation, cooling accounts for 8 % of the global CO₂ equivalent emissions¹. Switching to climate-friendly refrigerants and improving the energy efficiency of cooling appliances are the key challenges the cooling sector is facing in the fight against climate change [1].

Magnetocaloric cooling involves no environmentally critical gases and has the potential to increase efficiency by 40 %, as indicated by measurements of the coefficient of performance (COP) [4]. Temperature spans are generated with magnetocaloric materials (MCMs), which change their temperature when a magnetic field is applied or removed. This is commonly achieved by rotating permanent magnet assemblies, that cyclically magnetize and demagnetize the MCM. The heat transfer

is accomplished by a heat transfer fluid – usually water – which is pumped according to the magnetization and demagnetization phases.

A variety of different permanent magnet assemblies are known from the literature, e.g., [5, 6, 7, 8]. In this work, the interest lies particularly in the structural optimization of an axial rotary system design, as initially proposed by Okamura et al. [9]. Axial rotary systems have the advantageous property of linear scalability in the axial direction (neglecting edge effects), making them a favorable choice for commercialization.

At present, commercial vapor-compression systems are more than a hundred years ahead in research and development [10]. Thus, simulation and optimization are fundamental tools to rapidly improve magnetocaloric cooling devices and make them competitive in terms of power density and efficiency. Here, this is achieved with the use of Isogeometric Analysis (IGA). Being able to model geometries exactly and to apply shape optimization in a straightforward way are particular advantages of IGA. As a result, IGA has successfully been applied to model and optimize rotating machines [11].

The structure of this paper is as follows: Section 2 gives insights to the underlying geometrical and physical modeling. In Section 3, an optimized magnet design for the rotor is generated with topology and shape optimization. Section 4 presents studies for the torque and the magnetic flux density. The work is concluded in Section 5.

¹Calculated with data from [2] and [3] in 2016

¹Calculated with data from [2] and [3] in 2016

2. Methodology

2.1. Geometric modeling

For the simulation of physical problems, the geometry needs to be represented. Classically, in the Finite Element Method (FEM), this is often done using a mesh of lowest order, e.g., triangles or tetrahedra. More detailed geometries, i.e., a finer mesh, lead to higher computational efforts and less detailed ones to larger geometrical and numerical errors. Thus, there is always a trade-off between computational cost and model accuracy. One way to resolve this problem is to use the CAD basis functions, i.e., B-Splines and Non-Uniform Rational B-Splines (NURBS), to represent complex geometrical structures exactly even within the FEM.

B-Spline basis functions \hat{B}_i^p are defined by their degree p as well as the knot vector

$$\Xi = \{\xi_1, \xi_2, \dots, \xi_{n+p+1}\}, \quad (1)$$

and can be calculated using Cox-de Boor's recursion formula [12]. The number of basis functions n results from p and Ξ . NURBS basis functions are constructed by weighting each B-Spline basis function \hat{B}_i^p with a additional weight w_i as

$$\hat{N}_i^p(\hat{x}) = \frac{w_i \hat{B}_i^p(\hat{x})}{\sum_{j=1}^n w_j \hat{B}_j^p(\hat{x})}, \quad (2)$$

for $\hat{x} \in \hat{\Omega} \subset \mathbb{R}$, where $\hat{\Omega} = [\xi_1, \xi_{n+p+1}]$ is the reference domain. Multivariate B-Spline and NURBS basis functions can be defined using a tensor-product approach. To describe a 1-dimensional manifold $\Omega \subset \mathbb{R}^d$ in the d -dimensional physical space as a NURBS curve, each basis function is associated with a control point $\mathbf{P}_i \in \mathbb{R}^d$ via multiplication. The curve parametrization is then given by

$$\mathbf{F} : \hat{\Omega} \rightarrow \Omega, \quad \mathbf{x} = \mathbf{F}(\hat{x}) := \sum_{i=1}^n \mathbf{P}_i \hat{N}_i^p(\hat{x}). \quad (3)$$

Surfaces and volumes can be defined similarly using multivariate basis functions and a mesh of control points.

This allows for the exact representation of conic sections, such as circles or ellipses, which is particularly useful for rotating machines, such as the one shown in Fig. 1. The working principle of this exemplary axial rotary cooling device will be explained in the following chapters.

2.2. Magnetostatics

When modeling magnetic machines, it is often sufficient to only consider simplified approximations of Maxwell's equations. Here, nonlinear material behavior and time dependent phenomena such as eddy currents are neglected. The magnetic vector potential formulation [13]

$$\nabla \times (\nu(\nabla \times \mathbf{A} - \mathbf{B}_r)) = \mathbf{J}, \quad (4)$$

then describes the magnetic field, where the magnetic vector potential \mathbf{A} is defined such that the magnetic flux density is

$$\mathbf{B} = \nabla \times \mathbf{A}. \quad (5)$$



Figure 1: Exemplary magnet assembly of an axial rotary cooling device. Published with kind permission from Christian Vogel.

Furthermore, $\nu = \mu^{-1}$ is the (potentially anisotropic) reluctivity, i.e., the inverse permeability, \mathbf{B}_r the remanence of the permanent magnets and \mathbf{J} the electric current density. Here, all variables are assumed to be space-dependent. The linear material law

$$\mathbf{B} = \mu \mathbf{H} + \mathbf{B}_r \quad (6)$$

is used to model the relation between the magnetic field strength \mathbf{H} and magnetic flux density \mathbf{B} considering the remanence of the material.

In the following, we assume that the geometry is sufficiently long in axial direction and has no cross-sectional changes, such that magnetic fields in the z -direction are negligible. We therefore restrict ourselves to two dimensional magnetostatic modeling and simulations.

2.2.1. Magnetostatics for 2D

By assuming $\mathbf{A} = [0 \ 0 \ A_z]^\top$ for the 2D-case, (4) simplifies to the Poisson problem [14]

$$-\nabla \cdot (\nu^\perp (\nabla A_z - \mathbf{B}_r^\perp)) = J_z \quad (7)$$

with the anisotropic reluctivity

$$\nu^\perp = \frac{\boldsymbol{\mu}^\top}{\det(\boldsymbol{\mu})} \in \mathbb{R}^{2 \times 2}, \quad (8)$$

where $\boldsymbol{\mu}$ is also reduced to 2D. In the isotropic case, (8) further simplifies to $\nu = \mu^{-1} \in \mathbb{R}$. The variable \mathbf{B}_r^\perp contains the perpendicular components of the remanence and is defined as

$$\mathbf{B}_r^\perp = \begin{pmatrix} -B_{ry} \\ B_{rx} \end{pmatrix}. \quad (9)$$

The magnetic flux density is then calculated from (5) as

$$\mathbf{B} = \begin{pmatrix} \partial A_z / \partial y \\ -\partial A_z / \partial x \end{pmatrix}. \quad (10)$$

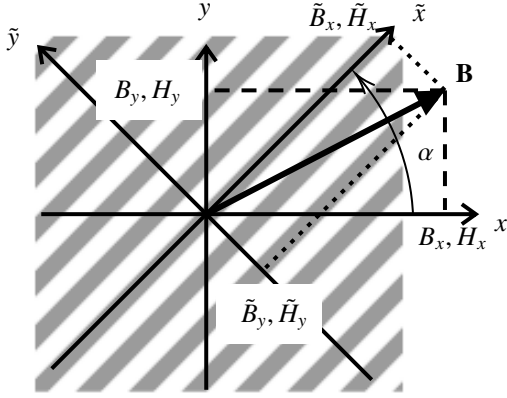


Figure 2: Visualization of a rotated two phase material in an arbitrary magnetic field.

2.2.2. Magnetocaloric material model

Implementing an active magnetic regenerator (AMR) is the most common way to create larger temperature spans in magnetocaloric cooling. The AMR consists of a small-scale MCM structure which is in contact with the heat transfer fluid. The geometry of the MCM is either classified as *packed bed* or *ordered structure* [15]. Common examples are packed spheres or parallel plates, respectively. The feature size of the MCM is usually below 1 mm in order to ensure a good heat transfer between the solid material and the perfusing fluid.

To account for the anisotropic behavior of such microstructures, the analytic Voigt and Reuss bounds for the permeability are used to determine the edge cases of the material behavior [14]. The Voigt-case corresponds to a layered material with the different phases arranged in the direction of the magnetic field and defines the upper limit for the permeability as

$$\mu_{\text{Voigt}} = (f_1\mu_1 + f_2\mu_2) = \langle \mu \rangle, \quad (11)$$

where f_1 and f_2 are the volume fractions and $\langle \cdot \rangle$ denotes the averaged value. The Reuss-case corresponds to a layered material with the phases arranged perpendicular to the magnetic field and defines the lower bound for the permeability as

$$\mu_{\text{Reuss}} = \left(\frac{f_1}{\mu_1} + \frac{f_2}{\mu_2} \right)^{-1} = \langle \mu^{-1} \rangle^{-1}. \quad (12)$$

In the case of parallel phases rotated by the angle α , as shown in Fig. 2, the effective permeability tensor $\boldsymbol{\mu}$ is obtained by applying

$$\boldsymbol{\mu} = \mathbf{R}_\alpha \tilde{\boldsymbol{\mu}} \mathbf{R}_\alpha^{-1}. \quad (13)$$

This describes the coordinate transformation to the known unrotated reference system by the rotation matrix

$$\mathbf{R}_\alpha = \begin{pmatrix} \cos(\alpha) & -\sin(\alpha) \\ \sin(\alpha) & \cos(\alpha) \end{pmatrix}. \quad (14)$$

The permeability in the reference system $\tilde{\boldsymbol{\mu}}$ is given by the Voigt and Reuss limits with

$$\tilde{\boldsymbol{\mu}} = \begin{pmatrix} \mu_{\text{Voigt}} & 0 \\ 0 & \mu_{\text{Reuss}} \end{pmatrix}, \quad (15)$$

using (11) and (12).

2.3. Numerical methods

2.3.1. Isogeometric Analysis

In the context of the FEM, Isogeometric Analysis (IGA) is a technique which uses B-Splines and NURBS to represent both geometry and solution of the partial differential equation (PDE). In the case of 2D magnetostatics, the magnetic vector potential A_z is parametrized with n ansatz functions $N_i(\mathbf{x})$ and coefficients u_i as

$$A_z(\mathbf{x}) = \sum_{i=1}^n N_i(\mathbf{x}) u_i. \quad (16)$$

To flexibly represent the permanent magnets, the same parametrization is applied here to the remanence \mathbf{B}_r , expressing the x - and y -component as

$$B_{rx}(\mathbf{x}) = \sum_{i=1}^n N_i(\mathbf{x}) b_i^{(x)}, \quad B_{ry}(\mathbf{x}) = \sum_{i=1}^n N_i(\mathbf{x}) b_i^{(y)}, \quad (17)$$

with coefficients $b_i^{(x)}$ and $b_i^{(y)}$, respectively.

Expressing both geometry and solution as NURBS and B-Splines makes IGA also a powerful tool for shape optimization, as (almost) arbitrary modifications of the geometry are possible by adjusting the coordinates of the control points without having to remesh the model [16, 17].

2.3.2. Implementation of rotation

In the context of IGA, harmonic mortaring has been proposed to efficiently simulate rotating electric machines, see, e.g., [16, 18, 19]. This method is also suitable for the case of a magnetocaloric cooling device. Instead of remeshing each rotor position, the boundaries of the rotating structures are coupled by harmonic (Fourier) basis functions. This allows for the use of non-conforming geometries at the coupling boundary which reduces the computational simulation effort.

To this end, we define the domains Ω_{rt} for the rotating part, Ω_{st} for the stationary part and the boundary Γ_{ag} , which represents the interface in the air gap between the rotor and stator. In Fig. 12, Γ_{ag} corresponds to the circle in the air gap between the AMRs and the rotor. In the domains, the magnetostatic equation (7) must be fulfilled, which simplifies to

$$\begin{cases} \nabla \cdot (\mu_{rt}^{-1} \nabla A_{z,rt}) = \mu_{rt}^{-1} \nabla \cdot \mathbf{B}_r^\perp & \text{in } \Omega_{rt} \\ \nabla \cdot (\mu_{st}^{-1} \nabla A_{z,st}) = \mu_{st}^{-1} \nabla \cdot \mathbf{B}_r^\perp & \text{in } \Omega_{st}, \end{cases} \quad (18)$$

assuming isotropic material properties and no excitation currents. On the coupling boundary Γ_{ag} , the two conditions

$$\begin{cases} A_{z,st}(\theta) = A_{z,rt}(\theta - \beta) & \text{on } \Gamma_{ag} \\ H_{\theta,st}(\theta) = H_{\theta,rt}(\theta - \beta) & \text{on } \Gamma_{ag}, \end{cases} \quad (19)$$

must be fulfilled, where θ is the angle used for evaluation and β the rotation angle. The field quantities are evaluated in their respective local coordinate system, see [18]. H_θ denotes the azimuthal component of the magnetic field strength and is given by

$$\begin{cases} H_{\theta,rt} = -\mu_{rt}^{-1} \nabla A_{z,rt} \cdot \mathbf{n}_{rt} \\ H_{\theta,st} = \mu_{st}^{-1} \nabla A_{z,st} \cdot \mathbf{n}_{st} \end{cases} \quad (20)$$

with the outward pointing normal vectors \mathbf{n}_{rt} and \mathbf{n}_{st} . Discretization of (18) with the standard Ritz-Galerkin approach using B-Spline ansatz functions and the parametrization of (19) and (20) using harmonic basis functions leads to the coupled system

$$\begin{pmatrix} \mathbf{K}_{rt} & 0 & -\mathbf{G}_{rt} \\ 0 & \mathbf{K}_{st} & \mathbf{G}_{st} \\ -\mathbf{G}_{rt}^T & \mathbf{G}_{st}^T & 0 \end{pmatrix} \begin{pmatrix} \mathbf{u}_{rt} \\ \mathbf{u}_{st} \\ \lambda \end{pmatrix} = \begin{pmatrix} \mathbf{b}_{rt} \\ \mathbf{b}_{st} \\ 0 \end{pmatrix}, \quad (21)$$

which is a saddle point problem as known from the literature [20]. Here, the stiffness matrix \mathbf{K} , the discrete solution vector for the magnetic vector potential \mathbf{u} , and the contribution of the permanent magnets \mathbf{b} are separated on the domains Ω_{rt} and Ω_{st} . Further details on the coupling matrices \mathbf{G}_{rt} , \mathbf{G}_{st} and the coupling coefficients λ can be found in [19, 18].

Using this formulation, the torque can be directly computed using the Lagrange multipliers λ , as explained in [19].

3. Structural optimization

Structural optimization is typically classified into the three types *parameter*, *topology* and *shape* optimization [21]. For a given geometry, parameter optimization is used to determine optimal (geometric) parameters, such as width, height or radius (Fig. 3a). In the case of topology optimization, the aim is to find novel designs, e.g., by assigning local (pseudo) density values for solid and void regions. This allows for adding or removing holes in the geometry (Fig. 3b). The result serves as draft for a specific structural setting. Given the basic topology, shape optimization can be used to adjust the boundary of the geometry. In the case of IGA, this can be achieved by moving control points that define the boundary (Fig. 3c).

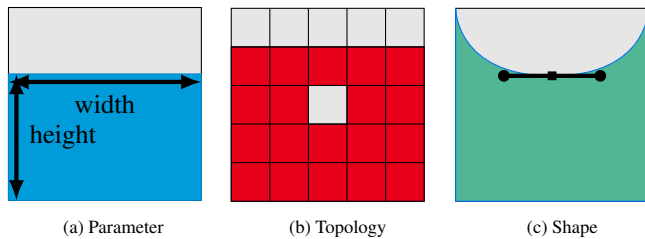


Figure 3: Types of structural optimization.

In this work, topology optimization is first used to determine the best topological layout. Shape optimization is then applied to further homogenize the magnetic field.

3.1. Topology optimization

Research concerning the topology of magnet assemblies to date usually assumes a fixed remanence direction given by Halbach cylinders [8, 22]. This work proposes a more general design approach, where the local remanence may change its magnetization direction, allowing for novel designs to be created.

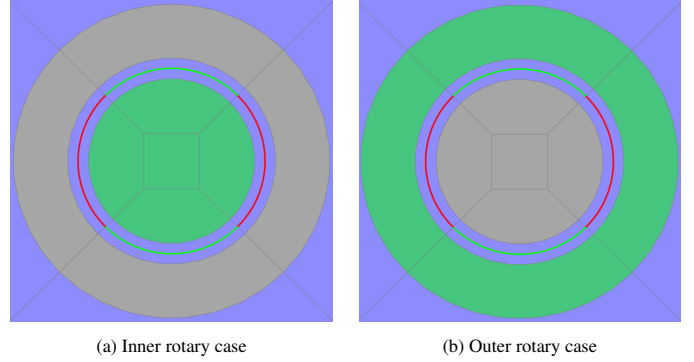


Figure 4: Design areas for the inner and outer rotary case. The green patches indicate the design area for the topology optimization. $\langle B_{\text{high}} \rangle$ and $\langle B_{\text{low}} \rangle$ are obtained by evaluation of the indicated red and green points.

3.1.1. Methodology

Larger changes in the magnetic field induce higher temperature changes in the MCM. Hence, it is necessary to have a high magnetic flux density in the air gap during magnetization and a near-zero magnetic flux density during demagnetization. Consequently, the objective function is chosen to maximize the difference of the average magnetic flux density during magnetization $\langle B_{\text{high}} \rangle$ and the average magnetic flux density during demagnetization $\langle B_{\text{low}} \rangle$. Here, a symmetric operation of the AMRs for a two-pole refrigerator is assumed, i.e., the (de)magnetization phases are equally sized to simplify operation and assembly of the system.

Moreover, only rotating permanent magnets are investigated, as rotating AMRs have shown disadvantages regarding the hydraulic system and sealing friction [23]. The design areas for the topology optimization are shown as green patches in the Figs. 4a (inner rotary) and 4b (outer rotary). Gray and blue patches represent iron and air, respectively. The combination of both design areas leads to the co-rotational case. The magnetic flux density in the air gap is evaluated at equidistant points indicated in green (B_{high}) and red (B_{low}). For the inner radius, air gap thickness and outer radius, $r_i = 40$ mm, $d_{\text{ag}} = 10$ mm and $r_o = 75$ mm are used, respectively. However, these values can be scaled without influencing the distribution of the magnetic flux density due to the scale independence of magnetic fields in the absence of currents or charges [24].

The remanence \mathbf{B}_r in the design area is discretized according to (17). The coefficients $b_i^{(x)}$ and $b_i^{(y)}$ are the design variables and will be modified during the optimization. Depending on the absolute value of \mathbf{B}_r , the material behavior resembles either a permanent magnet or soft iron.

Two additional constraints need to be imposed. First, the remanence is limited to a physically feasible value $B_{r,\text{mag}}$. Second, the remanent area, which correlates with the volume of the permanent magnet, is restricted by A_{max} to allow for an effective comparison between different designs. The resulting PDE-

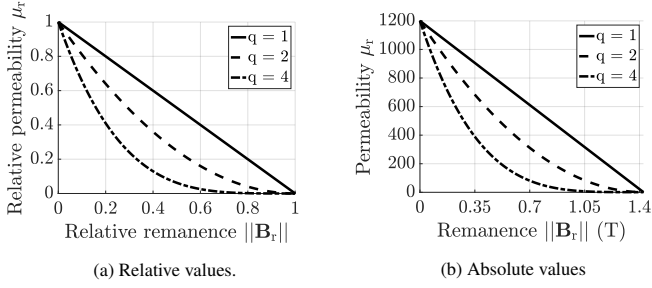


Figure 5: SIMP relationship to couple remanence and permeability to allow for the continuous transition from soft iron to permanent magnet regions. Intermediate values are penalized with increasing q .

constrained optimization problem reads

$$\max_{\mathbf{B}_r} f_{\text{opt}} = \langle B_{\text{high}} \rangle - \langle B_{\text{low}} \rangle \quad (22)$$

$$\text{s.t. } \|\mathbf{B}_r\| \leq B_{r,\text{mag}}, \quad (23)$$

$$\int_{\Omega} \|\mathbf{B}_r\| d\Omega \leq B_{r,\text{mag}} A_{\text{max}}, \quad (24)$$

$$\text{and (7) discretized with IGA.} \quad (25)$$

In mechanical topology optimization, the elastic modulus is coupled by a Solid Isotropic Material with Penalization (SIMP) relationship to describe the transition from solid to void [25]. In analogy, an adapted SIMP approach is used in this work to couple remanence and permeability of the material to distinguish between magnet and soft iron. This is possible, as soft iron has a high permeability and no remanence, whereas permanent magnets have low permeability and high remanence. The relationship is modeled as a decreasing function

$$\mu_{\text{rel}} = (1 - \|\mathbf{B}_r\|_{\text{rel}})^q, \quad (26)$$

where q is the penalization factor to avoid intermediate values of the material density in the topology optimization. The relative values for the remanence $\|\mathbf{B}_r\|_{\text{rel}} \in [0, 1]$ and the relative permeability $\mu_{\text{rel}} \in [0, 1]$ are obtained by a linear mapping between the minimum and maximum values, which are given by the magnet and soft iron. Relative permeabilities of $\mu_{r,\text{iron}} = 1200$ and $\mu_{r,\text{pm}} = 1.05$ are used for soft iron and permanent magnet, respectively. The remanence limits are set to zero for iron and $|B_{r,\text{mag}}| = 1.425$ T for the magnet, which is achievable, e.g., with Nd-Fe-B magnets. This dependence is demonstrated for different penalization factors in Fig. 5. Here, a value of $q = 4$ has shown to be appropriate.

3.1.2. Results

The implementations are made in MATLAB[®] using the open source packages *NURBS* [26], *Tensor Toolbox* [27] and *GeoPDEs* [28, 29] as well as the MATLAB[®] *Optimization toolbox* [30].

All optimization steps are performed with sensitivity analysis and analytical derivations of the gradient information. The adjoint method [21] is used to derive the gradient of the objective function and constraints with respect to the remanence coefficients $b_i^{(x)}$ and $b_i^{(y)}$. The optimization is then realized with

the *interior-point* method from the MATLAB[®] solver *fmincon*. For comparability, 100 iterations are performed in each optimization. This achieves efficient computation and convergence within 30 minutes for each optimization on a PC with an Intel Dual Core i7-4600U processor and 8 GB of RAM.

Due to the nature of gradient based algorithms, the initial conditions influence the convergence process and hence the final solution. This is demonstrated for the inner rotary design in the Figures 6 and 7. The dark blue areas indicate non-remanent regions, which behave like soft iron. Yellow areas are assigned the properties of a permanent magnet, where the remanence direction is given by the black arrows. Intermediate values are plotted in the color range in between.

To magnetize the air gap, the remanence can be either directed from bottom to top or vice versa. Due to this symmetry, the gradient is zero if all-zero initial conditions are provided, as this corresponds to a saddle point of the objective function. In Fig. 6a, a small value is assigned to the remanence of the center patch. As the patches aligning with the air gap have the highest contribution to the objective function, the remanence is increased exactly there during the iterations (Fig. 6b). During the optimization process, intermediate values are removed and more material becomes remanent (Fig. 6c), until the specified maximum magnetic area is reached (Fig. 6d), resulting in the *inner rotary top and bottom* design, similar to the one in [31]. For its realization, sintered magnets are needed, where the magnetization is uniformly approximated.

When using slightly different initial conditions with a remanent value of $|\mathbf{B}_r| = 0.85$ T (Fig. 7a), the solver converges to a second possible design, the *inner rotary centered* design. Increasing the remanence at the areas of the air gap in this case would also decrease the permeability there and therefore impede the already existing magnetic flux. Instead, creating a remanent arc (Fig. 7b) increases the objective function faster. After several iterations (Fig. 7c), the centered design is obtained (Fig. 7d). Building it requires multiple magnet segments and the omission of a continuous shaft, making the assembly complex. At the same time, replacing the shaft is crucial to remove the parasitic backflow of magnetic flux through the shaft, seen in designs from the literature [32].

Carrying out this optimization process also for the outer- and co-rotational cases yields four different design possibilities, given in Fig. 8. In the *outer rotary* design (Fig. 8c), permanent magnet material is positioned at the transition zones from magnetization to demagnetization to generate a sharper distinction for the high and low magnetic field areas. The *co-rotational* design (Fig. 8d) combines the inner and outer rotary cases.

Repeating this optimization process for varying permissible permanent magnet volume or – in 2D – cross-section area A_{max} with the four design variants yields the results presented in Fig. 9. Note that the x -axis shows the relative area $A_{\%} = A_{\text{max}}/A_{\text{inner}}$ of the permanent magnets in relation to the inner area A_{inner} from Fig. 4a to enable a comparison of the designs. Summarizing the most important findings from Fig. 9, we see that:

- For low magnetic areas, the *inner rotary top and bottom*

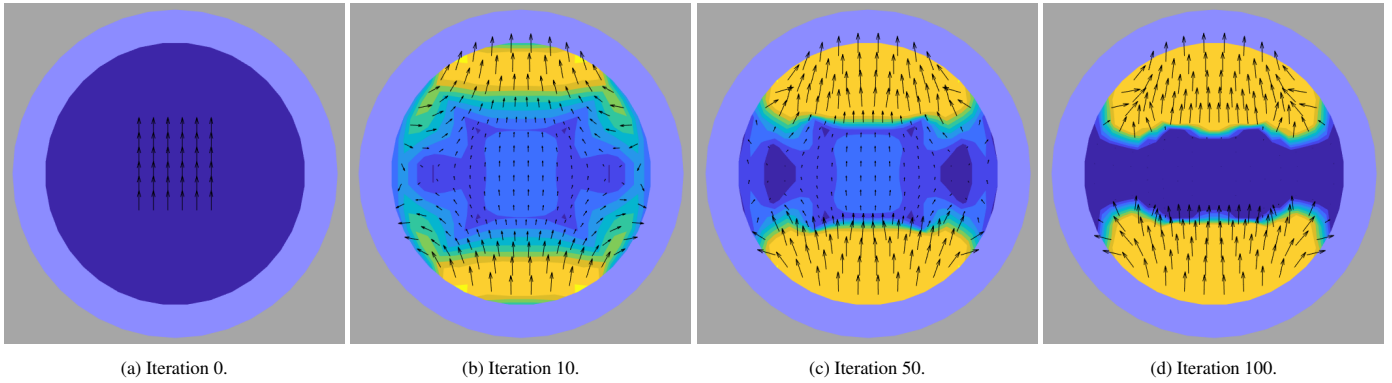


Figure 6: Optimization steps for the top and bottom inner rotary design. Yellow areas indicate permanent magnet material, deep blue and gray areas represent soft iron. A low B_r of 0.02 T in the center patch prescribes the magnetization direction in iteration 0. The areas directly aligning with the air gap have the highest contribution to the objective function and are increased in remanence, leading to a separated top and bottom design.

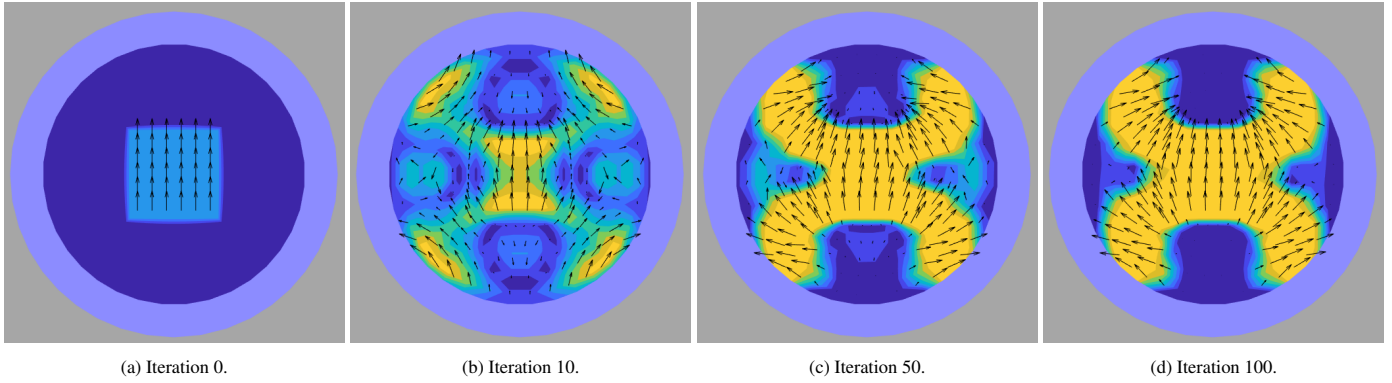


Figure 7: Optimization steps for the centered inner rotary design. Yellow areas indicate permanent magnet material, deep blue and gray areas represent soft iron. For a higher B_r of 0.85 T as initial condition for the center patch, the solver converges to a centered design. The already remanent area is used by adding further remanent material at the patch corners. The magnetic flux is then concentrated in the areas, which take the properties of soft iron.

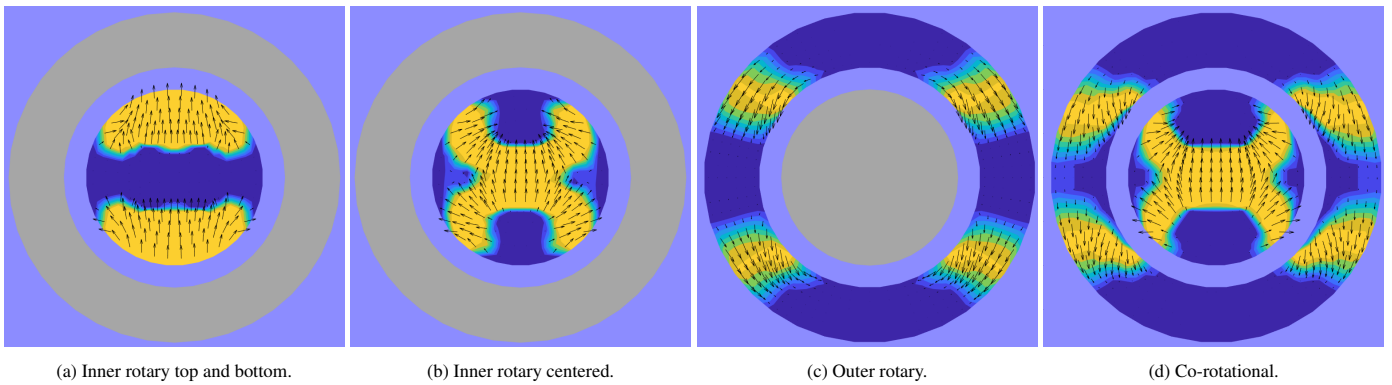


Figure 8: Topology optimization results for the inner rotary, outer rotary and co-rotational case. Yellow areas indicate permanent magnet material, deep blue and gray areas represent soft iron. For the inner rotary case, two solutions are found, depending on the initial conditions (Fig. 8a and 8b). In the outer rotary case (Fig. 8c), permanent magnet material is positioned at the transition zones from magnetization to demagnetization to generate a sharper distinction for high and low magnetic field areas. The co-rotational case (Fig. 8d) combines the inner and outer rotary case (also depending on initial conditions).

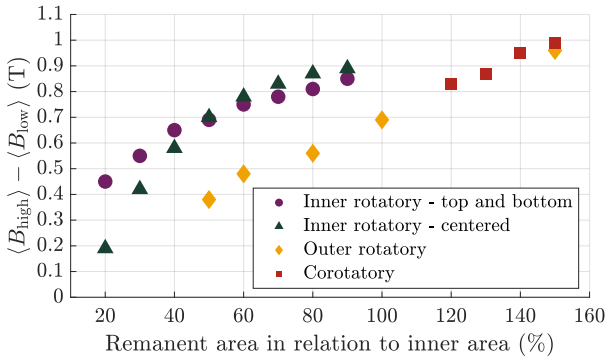


Figure 9: Comparison of the inner, outer and co-rotational design variants. The objective value (22) is compared for the four design variants, given in Fig. 8. The inner design area from Fig. 4a is used as reference for the comparison.

design performs best. If the magnet area is severely restricted, putting the magnets exactly where needed yields the best results.

- For magnetic areas of $A_{\%} \geq 50\%$, the *inner rotary centered* design outperforms the *top and bottom* one. With higher proportion of permanent magnets, the concentration of the magnetic flux proves advantageous.
- The *outer rotary* design yields the lowest objective values for all cases, as explained by the unfavorable scaling in the radial direction.
- The overall highest objective values are reached with a *co-rotational* design, as to be expected. It is important to note that the co-rotational case is not a superposition of the inner and outer rotary cases due to the low permeability of permanent magnets, which impedes the magnetic flux. Such high magnetic fields therefore come at the cost of a significantly higher permanent magnet volume.

When applying the optimization method to an adapted problem with a different number of poles or a large outer diameter, further interesting results are found:

- Some articles feature a design with four magnetic poles [33, 7]. This has been tested, but the objective values are found to be 15 to 30 % smaller compared to a two pole design. It is therefore recommended to prefer two pole systems operated at higher frequency.
- For large outer diameters, an outer rotary magnet design with magnets adjacent to the air gap similar to [34, 35] is found (top right yellow diamond in Fig. 9). However, such an assembly is discouraged for commercial applications due to high space and permanent magnet mass requirements.

3.2. Design implementation

Assuming that geometries similar to the ones obtained from the topology optimization yield a comparable magnetic flux

density, the *inner rotating centered* design (Fig. 8b) is chosen as most suitable initial topology for further optimization.

The *inner rotary top and bottom* design is more efficient at low magnet mass, but with current MCM technology, higher magnetic fields are needed. The *co-rotational* design yields higher objective values, but this is at the expense of a drastically larger magnet mass and a higher complexity of the assembly. This design is only recommended for applications where a higher power density is necessary. Overall, the *inner rotary centered* design is a good compromise between a high magnetic flux density and comparatively low permanent magnet mass. If needed, this design can be extended to a co-rotational one.

Figure 10a shows the simplified geometry created based on the topology optimization. The green patches indicate permanent magnets with the magnetization direction given by the arrows. The gray and blue patches indicate soft iron and air, respectively. The shapes of the permanent magnets are chosen in a way that allows an efficient production. In particular, the magnets can be easily cut from rectangular segments. The one remaining challenge with this design is to ensure the concentricity of the assembly in the absence of a continuous shaft.

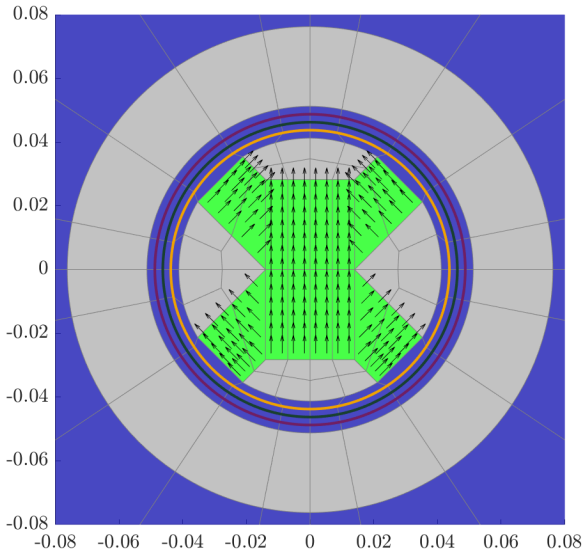
The resulting magnetic flux density is shown in Fig. 10b. With a share of $A_{\%} = 60\%$ of permanent magnets in the rotor, an objective value of $|\mathbf{B}| = 0.76\text{ T}$ is obtained, which is in very good agreement with the predicted value from the topology optimization. Figure 11 shows the evaluation of the magnetic flux density in the air gap around the circles at $r = 42.5, 45$ and 47.5 mm (see colored lines in Fig. 10a). At the center radius, the magnetic flux density is constant during magnetization with a value of $|\mathbf{B}| = 0.96\text{ T}$. In the radial direction, the magnetic flux density decreases as the flux is distributed across more space. At the inner radius, peaks in the magnetic flux density are observed.

The magnetic flux density in the air gap is verified by nonlinear simulations carried out in COMSOL Multiphysics®, which show maximum differences of less than 0.1 %. Errors due to neglecting of saturation effects turn out to be smaller than 0.5 %, which also justifies to carry out the optimizations with linear material properties.

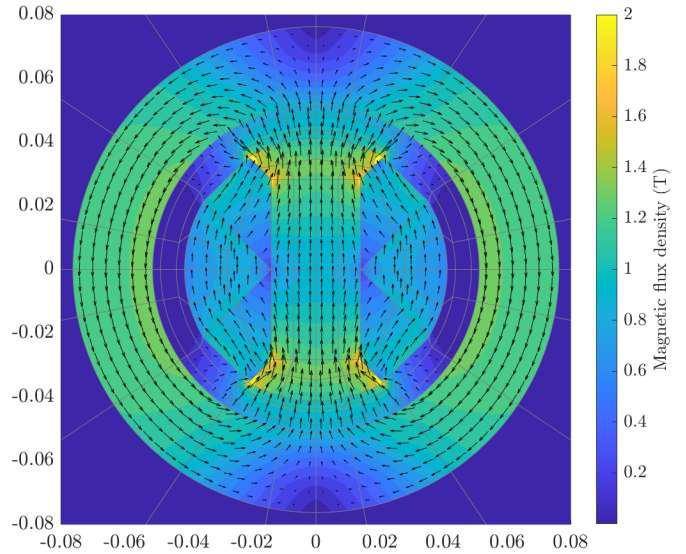
Usually, the coefficient Λ_{cool} is used as reference when comparing magnetocaloric cooling assemblies [5]. With a magnetic area of 31.9 cm^2 , an air gap area of 29.8 cm^2 , of which one third is magnetized, $\langle B_{\text{high}}^{0.7} \rangle = 0.97\text{ T}$, $\langle B_{\text{low}}^{0.7} \rangle = 0.03\text{ T}$ and $P_{\text{field}} = 0.75$, it follows that $\Lambda_{\text{cool}} = 0.219$ and $\Lambda_{\text{cool}}/P_{\text{field}} = 0.29$. These values are even higher compared to the ones provided in the literature [5]. Here, these values are given only for comparison as Λ_{cool} has some drawbacks, e.g., it does not consider MCM cost, cooling power or the device efficiency [36]. An even higher Λ_{cool} could be achieved here with an increasing air gap. It has therefore been proposed to include $B^{4/3}$ in such merit figures [37].

3.3. Shape Optimization

Measurements on a magnetocaloric device indicate that peaks in the magnetic flux density during the magnetization reduce the performance of the MCM [38]. A lower but more homogeneous magnetic field performed significantly better than



(a) Geometry based on the topology optimization for the inner rotary centered design from Fig. 8b. The lines in the air gap are used to evaluate the magnetic flux density.



(b) Magnetic flux density in Tesla. For the final evaluation, the soft iron is implemented with a B-H-curve using fixpoint iteration.

Figure 10: Deduced geometry and analysis of the magnetic flux density.

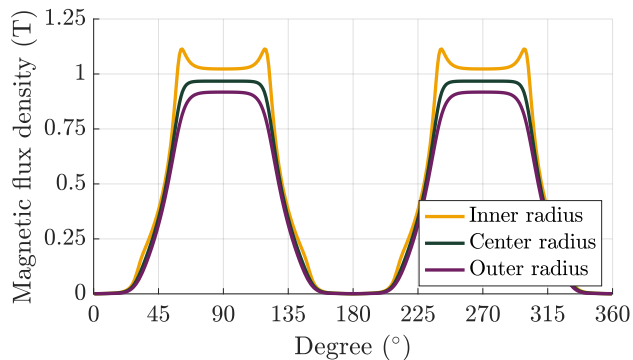


Figure 11: Magnetic flux density in the empty air gap, evaluated at the lines indicated in Fig. 10a.

a higher, inhomogeneous one. In [38], the authors stated that these peaks create “parasitic thermodynamic cycles” and “represent additional irreversibilities”. Also in Fig. 11, we observe peaks during magnetization at the inner evaluation radius. To address this issue at an early design stage, shape optimization is applied to the soft iron parts of the geometry in order to remove the peaks in the magnetic flux density.

3.3.1. Methodology

So far, the influence of the MCM has widely been neglected, as the standard material for scientific prototypes, Gadolinium, reaches saturation very quickly and behaves similarly to air regarding the resulting magnetic field. As this device is aimed for commercialization, Gadolinium is not an option due to its high cost. Current MCM candidates for commercialization are alloys based on Lanthanum, Iron and Silicon (La-Fe-Si), which have a higher permeability. Thus, neglecting the MCM’s influence is not an option.

While some measurements of magnetization curves exist [39], the behavior of the MCM depends on many factors, such as the ambient and Curie temperatures. We therefore use a worst case estimate for the permeability to investigate this problem. Assuming a conservative relative permeability of $\mu_{r,MCM} = 500$ and a volume fraction of 60% for the MCM with water as second phase with $\mu_{r,water} = 1$, the upper limit of the permeability is given by the Voigt bound (11) as $\mu_{voigt} = 300$, which corresponds to parallel plates. For packed spheres, μ_r is consequently smaller, so we use an isotropic $\mu_{r,AMR} = 200$ for the AMRs to simulate the edge cases of the macroscopic behavior.

The aim is again to maximize $\langle B_{high} \rangle - \langle B_{low} \rangle$, i.e., the difference in magnetic flux density between the magnetization and the demagnetization phase. The problem is defined in a similar way to the topology optimization as

$$\max_{\mathbf{P}} f_{opt} = \langle B_{high} \rangle - \langle B_{low} \rangle \quad (27)$$

$$\text{s.t. } \|\mathbf{P}_1\| \leq R_{max} \quad (28)$$

$$\|\mathbf{B}_{eval}(\beta_i)\| \leq \|\mathbf{B}_{eval}(\beta_{i-1})\| \quad (29)$$

$$\text{and magnetostatics (21) for all } \beta_i, \quad (30)$$

where this time the design variables are the control points \mathbf{P}_i of the geometry parametrization described in Section 2.1. Instead of evaluating multiple points in the air gap, one point in the MCM is evaluated for different rotation angles $\beta \in \{0, 1, \dots, 90\}$.² The values $\langle B_{high} \rangle$ and $\langle B_{low} \rangle$ are then obtained by averaging the magnetic flux density for the rotation angles during magnetization and demagnetization, respectively.

Again, constraints are needed. First, the control points are restricted by the radius R_{max} to ensure feasible designs. Second, the magnetic flux density at each previous evaluation angle β_{i-1} must be larger than the magnetic flux density at the

²The optimization has also been performed with an empty air gap, but since the results are very similar, only the results for a filled air gap are presented.

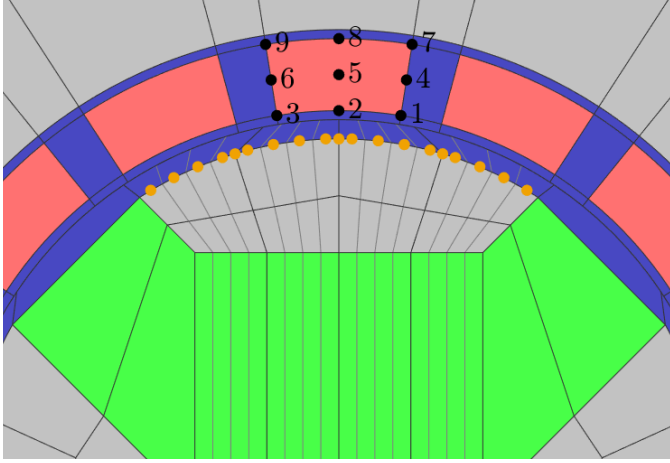


Figure 12: Initial geometry for the shape optimization. The orange points denote the control points, which serve as design variables.

current evaluation angle β_i . This is sufficient, because only one (de)magnetization process is simulated due to the symmetries. Consequently, the magnetic flux density must be monotonically decreasing and become more homogeneous, as peaks are infeasible.

The initial geometry is visualized in Fig. 12. The control points, which define the soft iron surface and act as design variables for the shape optimization, are shown in orange. Soft iron and magnets are again shown as gray and green patches, where the magnetization direction is the same as in Fig. 10a. Blue patches indicate air or any support material behaving like air. The magnetic flux density is evaluated at the black points in the AMR, which are the red patches. Point 2 is used to evaluate the magnetic flux density for the rotation angles from $\beta = 0^\circ$ to 90° in 1° steps. This simulates the process of the top center AMR from being fully magnetized to demagnetized.

The optimization is again realized with the MATLAB® solver *fmincon* using analytically derived gradients for the optimization function and constraints. For the shape optimization, the *SQP* method is used, as it converges faster for a low number of design variables and is better suited for infeasible points, since the initial condition violates the second constraint due to the peak.

3.3.2. Results

The iteration process for the shape optimization is shown in Fig. 14. Starting from a circular arc with its center at the coordinate origin as initial condition (Fig. 14a), the radius of the soft iron is increased in the center to yield a higher objective function and decreased at the left and right sides to avoid the peaks in the magnetic flux density (Fig. 14b). The solver quickly converges to a design where the distance of the AMR to the soft iron is slowly reduced (Fig. 14c), yielding a smooth transition of the AMR into the magnetization zone when the system rotates. Increasing the distance to the AMR at the magnet edges has also been shown to increase the magnetic flux density in other assemblies [40].

The magnetic flux density during the optimization process at

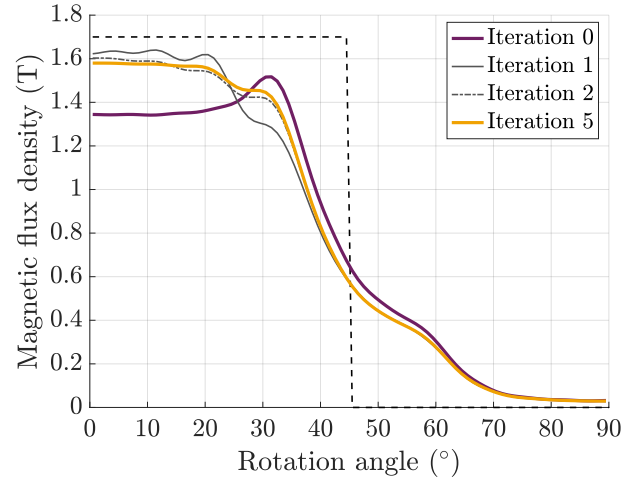


Figure 13: Magnetic flux density in the AMR over the course of the optimization. Starting with a peak in the initial design, the magnetic flux density is gradually homogenized during the optimization process, resulting in a higher and more uniform magnetic flux density.

the evaluation point is shown in Fig. 13. In the initial design, the magnetic flux is concentrated in the AMR part which has already entered the magnetization zone. As the whole AMR enters the magnetization zone, the magnetic flux density is distributed across the entire AMR volume. This effect results in a falling magnetic flux density in the AMR, causing the peaks during magnetization. For the optimized shape, the distance of the AMR to the soft iron changes during operation. The smaller distance at the center increases the magnetic flux density there and shifts the high concentration of the magnetic flux density to the center. The peaks during magnetization are therefore removed, leading to a more homogeneous magnetic field in the AMR. Note that the magnetic flux density in the AMR is simulated, resulting in a higher magnetic flux density in Fig. 13 compared to Fig. 11 due to the higher μ_r .

For a practical design, it is possible to approximate the spline geometry of the rotor well by a circular arc where the circle center is not the origin, but shifted in the y -direction. This may simplify the manufacturing process.

4. Final design studies

4.1. Torque study

For an efficient refrigeration system, it is essential to minimize occurring torques during operation to reduce the power consumption of the motor [41]. Also, the rotation becomes more stable and valve mistimings of the hydraulic system are less likely to occur.

As the magnetic flux is concentrated in the AMRs due to the increased permeability, the magnetic flux is not evenly distributed in the air gap, resulting in reluctance forces and torque. This depends mainly on the geometric configuration of the rotor and stator, i.e., the setup of the permanent magnets and the AMRs [42]. This is particularly important for devices aimed to be operated with La-Fe-Si, as the higher permeability leads to

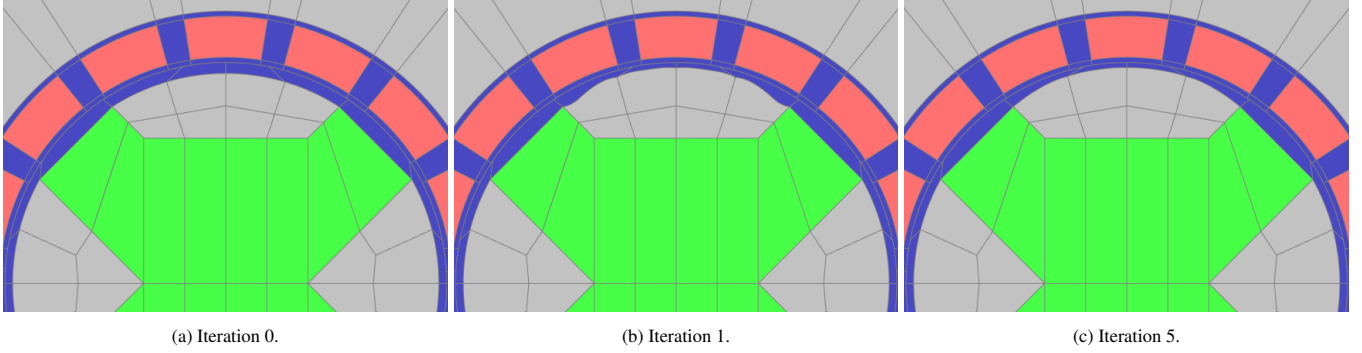


Figure 14: Shape optimization process for a filled air gap with simplified AMR properties. A circular arc with center at the coordinate origin is used as initial condition. In the first iteration, the solver increases the overall radius, except for the peak areas, where the AMR enters (or leaves) magnetization. There, the radius is decreased to remove the peaks in the magnetic flux density. After several iterations, the optimizer converges to a design, where the distance to the AMR is gradually decreased as the system rotates.

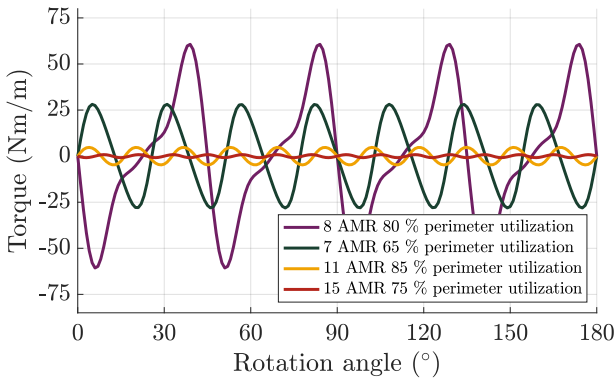


Figure 15: Exemplary torque curves for different stator setups, varying the number of AMRs and the share of MCM along the perimeter in the air gap.

torques several times higher compared to Gadolinium. We only examine the static holding torque (cogging torque) and neglect effects like eddy currents or friction.

The rotor geometry has already been determined with the topology optimization, so a parametrized stator geometry is analyzed with the initial rotor design from Fig. 12. There are two parameters that have a major influence on the cogging torque, that is, the number of AMRs n_{AMR} and the share of AMRs along the perimeter r_{AMR} (called perimeter utilization in the following). The AMRs are designed to be evenly distributed along the perimeter. Figure 15 shows exemplary torque curves for half a revolution. The values are calculated per unit length, so the length of the device needs to be multiplied for the real values. For an even number of AMRs, the number of maxima and minima corresponds to the number of AMRs. For an odd number of AMRs, there are twice as many maxima and minima, since the magnetic field at the poles is not symmetric. In this case, opposing sides do not necessarily contribute forces in opposite directions, resulting in considerably smaller torques.

Performing the torque simulations for a variety of parameter combinations yields the heat map presented in Fig. 16. The following observations are made:

- The most influential parameter is the number of AMRs

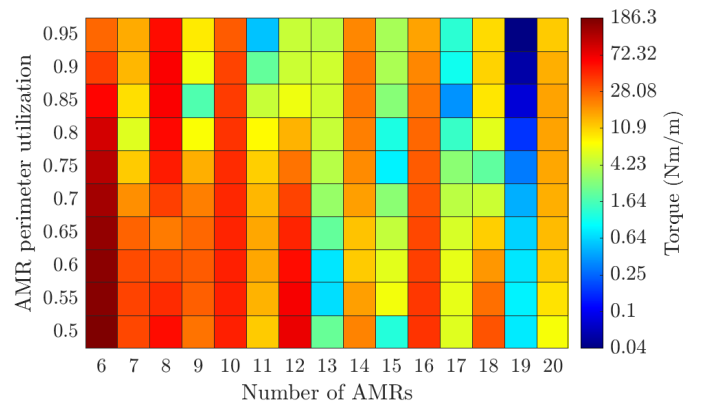


Figure 16: Holding torque per system length, depending on the number of AMRs and the perimeter utilization. Higher and odd numbers of AMRs correspond to lower torques.

n_{AMR} . Setups with an odd n_{AMR} have significantly lower torques than setups with an even n_{AMR} . A higher n_{AMR} also leads to lower torques.

- For a fixed n_{AMR} , there are again torque minima depending on r_{AMR} . They are explained by geometric setups, where one AMR enters the magnetization zone exactly when another one leaves.

Thus, in terms of torque, it is advisable to have an odd, high number of AMRs. Unless the MCM mass is not already determined by the specifications of the device, r_{AMR} can be further adjusted to reduce the torque.

4.2. Magnetic field evaluations

In the following, we present three different examples to highlight positive and negative design aspects. Note that these scenarios pose edge cases where the MCM permeability is overestimated to demonstrate its influence and to deduce general design rules.

The first example features a design with $n_{\text{AMR}} = 8$ AMRs and $r_{\text{AMR}} = 80\%$, where the AMRs are assumed to be isotropic with a constant relative permeability of $\mu_{r,\text{AMR}} = 200$, as explained

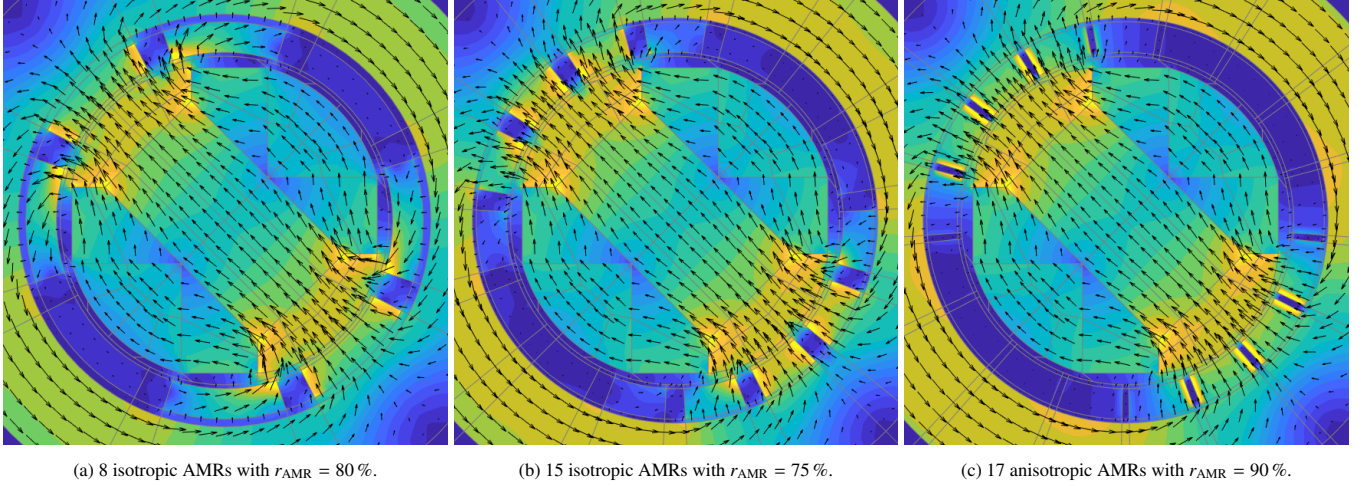


Figure 17: Magnetic flux density for three exemplary AMR designs. (a) An unfavorable design where the AMRs are too long, resulting in their magnetization, despite being only partially in the magnetization zone. (b) A favorable design with a higher n_{AMR} and lower r_{AMR} resulting in more distinct (de)magnetization zones. (c) A prospective scenario with both a high n_{AMR} and r_{AMR} . The magnetic flux is radially enforced due to the anisotropy of the AMRs, which allows distinct (de)magnetization zones and a high usage of MCM in the air gap.

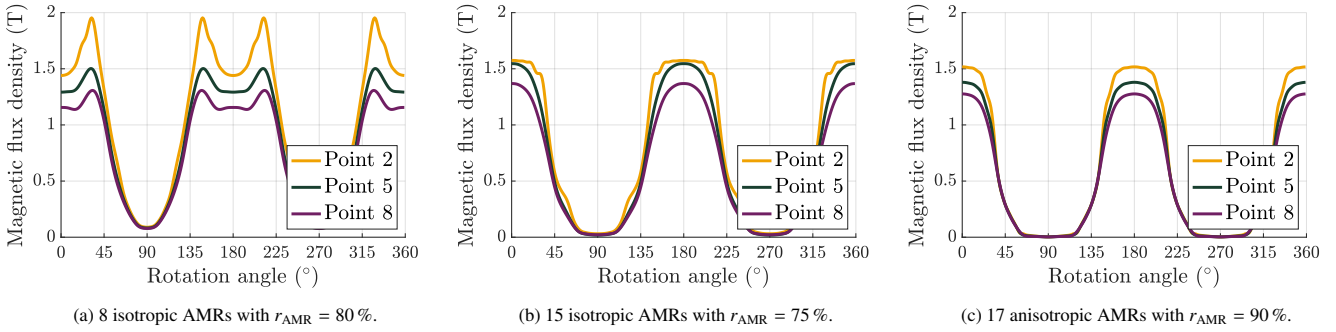


Figure 18: Magnetic flux density in the AMRs evaluated at the points given in Fig. 12. (a) An unfavorable design with high peaks in the magnetic flux density during the magnetization and a non-zero magnetic flux density during demagnetization. (b) A favorable design with a very homogeneous magnetic flux density during magnetization and a zero-field during demagnetization. (c) The highest MCM usage in the air gap and the most favorable magnetic flux density, which is reached with anisotropic AMRs.

in Section 3.3.1. A lower number of AMRs is sensible from a systemic point of view in order to simplify the hydraulic system. However, looking at the magnetic flux density in Fig. 17, we see that this design is not preferable from a magnetic field perspective for multiple reasons. First, the AMRs are too wide. This results in magnetization despite only being partially in the magnetization zone. Second, the high r_{AMR} leads to a parasitic backflow of the magnetic flux through the AMRs. This results in a very narrow demagnetization zone, where the magnetic flux density is not zero. Third, the magnetic flux is concentrated when the AMR enters the magnetization zone, which leads to high peaks. For wide AMRs, this cannot be resolved with shape optimization, which is why the optimized rotor for $n_{AMR} = 15$ AMRs is used for the evaluations. Last, the torque is very high due to the symmetric setup, as seen in Figs. 15 and 16.

A better approach is to use more AMRs and a lower perimeter utilization, as performed for the second design shown in Fig. 17b for $n_{AMR} = 15$ and $r_{AMR} = 75\%$. This ensures that the magnetic flux density in the AMRs is zero during demagnetization and there are no peaks during magnetization, as seen in

Fig. 18b. As a result, long (de)magnetization phases and a homogeneous flux density are achieved. In general, it is advisable to choose the width of the AMRs as well as the thickness of the air gap smaller than the width of the diagonal magnets to ensure the magnetic flux flow through the stator iron. Also note that the magnetic flux density in point 2 is exactly the final curve from Fig. 13, since it was optimized for this case. The torque is also very small, as seen again in Figs. 15 and 16. Another advantage of having more and smaller AMRs is that the shape can be simplified to a rectangle, which might be convenient for AMRs with ordered microstructures.

This case of anisotropic material behavior for the AMRs is investigated in the third example with $n_{AMR} = 17$ and $r_{AMR} = 90\%$. Assuming radially oriented phases, the radial and azimuthal permeability is calculated with (11) and (12) to $\mu_{r,AMR,rad} = 300$ and $\mu_{r,AMR,azi} = 2.5$ under the previous assumptions of $\mu_{r,MCM} = 500$ and a volume fraction of 60% for the MCM material. Generating this anisotropic behavior in reality could be realized with radially aligned plates or pins [43]. The permeability tensor for the AMRs is then given by

(13). The resulting magnetic field is shown in Fig. 17c. Despite having a high r_{AMR} , there is no magnetic flux during the demagnetization, as azimuthal flux is impeded by the microstructure. Clever exploitation of the MCM anisotropy leads to the fastest transition from the (de)magnetization phases and a homogeneous magnetic flux density, seen in Fig. 18c, regardless of whether the rotor is shape-optimized.

On the other hand, this analysis implies to avoid microstructures that obstruct the magnetic flux in radial direction. Measurements of parallel plated Gadolinium AMRs, where the cooling performance is found to be up to 40 % smaller for plates perpendicularly aligned to the magnetic field, support this theory [44]. This effect is assumed to be even stronger for materials with higher permeability such as La-Fe-Si, because the magnetic field is concentrated even more in phases with higher permeability. Using microstructures correctly therefore not only positively influences the magnetic field, but also concentrates the magnetic flux in the MCM phases, which enhances the temperature generation in the AMRs.

5. Conclusion

This paper introduces advanced simulation and optimization methods to find the most suitable design for an axial rotary magnet assembly for magnetocaloric cooling. Magnetostatic simulations are performed in an isogeometric analysis framework for an exact and flexible representation of the geometry, where the rotor and stator are coupled with harmonic mortaring. For efficient topology and shape optimization, analytical gradients have been used within the IGA framework. To account for the influence of the MCM, simple bounds have been applied to estimate the permeability for (an)isotropic materials.

The main findings can be summarized as follows:

- Based on the topology optimization results, an inner rotary magnet assembly is proposed as axial rotary design for commercial magnetocaloric refrigeration. To generate the large magnetic fields required for magnetocaloric cooling to date, it is suggested to build the geometry with five simple magnet segments and try to omit a continuous shaft. If necessary, this design can be extended to a co-rotational one.
- Inhomogeneous magnetic fields have shown to correlate with performance losses of the AMRs [38]. To avoid such problems, shape optimization has been applied to the rotor in order to homogenize the magnetic flux density in the AMRs. It has been shown that peaks in the magnetic flux density can be avoided for sufficiently small AMRs by adjusting the shape of the soft iron parts.
- A comprehensive torque study has been performed for a parametrized stator with equally spaced AMRs. We have seen that a high and odd number of AMRs is in general favorable for lower torques.
- Different positive and negative examples were evaluated with simplified assumptions for the MCM. Having a high

number of AMRs leads to a sharper distinction between the (de)magnetization phases. The best results are obtained with anisotropic AMRs that enforce the magnetic flux in radial direction.

For future research, it is recommended to further increase the modeling effort of the AMRs with a multiscale model that considers measurement data of the MCM. Also, the mechanical and hydraulic design need to be worked out in more detail in order to enable the assembly. One important geometry parameter that has yet to be determined is the width of the air gap. For this, more information about performance, efficiency and cost are needed.

The system presented will serve as a foundation for a manufacturing design that will be assembled and tested by the authors.

Acknowledgement

This work is supported by the joint DFG/FWF Collaborative Research Centre CREATOR (CRC – TRR361/F90) at TU Darmstadt, TU Graz and JKU Linz as well as the Graduate School CE within the Centre for Computational Engineering at TU Darmstadt. MAGNOTHERM thanks the EIC-Accelerator MCD under grant agreement number 190183588 for their financial support. Many thanks also to Christian Vogel for the fruitful discussions.

References

- [1] United Nations Environment Programme and International Energy Agency. Cooling emissions and policy synthesis report, 2020.
- [2] M. Roser H. Ritchie and P. Rosado. CO₂ and greenhouse gas emissions. *Our World in Data*, 2020. URL <https://ourworldindata.org/co2-and-other-greenhouse-gas-emissions>.
- [3] Green cooling initiative. Global greenhouse gas emissions from the rac sector. URL <https://www.green-cooling-initiative.org/country-data>.
- [4] C. Zimm et al. Description and performance of a near-room temperature magnetic refrigerator, 1998.
- [5] R. Bjørk, C.R.H. Bahl, A. Smith, and N. Pryds. Review and comparison of magnet designs for magnetic refrigeration. *International Journal of Refrigeration*, 33(3):437–448, 2010. ISSN 0140-7007. doi: 10.1016/j.ijrefrig.2009.12.012.
- [6] A. Kitanovski, J. Tušek, U. Tomc, U. Plaznik, M. Ožbolt, and A. Poredoš. *Magnetocaloric Energy Conversion*. Springer Cham. doi: 10.1007/978-3-319-08741-2.
- [7] R. Bjørk, C.R.H. Bahl, A. Smith, D.V. Christensen, and N. Pryds. An optimized magnet for magnetic refrigeration. *Journal of Magnetism and Magnetic Materials*, 322(21):3324–3328, 2010. ISSN 0304-8853. doi: 10.1016/j.jmmm.2010.06.017.
- [8] R. Teyber, P.V. Trevizoli, T.V. Christiaanse, P. Govindappa, I. Niknia, and A. Rowe. Permanent magnet design for magnetic heat pumps using total cost minimization. *Journal of Magnetism and Magnetic Materials*, 442: 87–96, 2017. ISSN 0304-8853. doi: 10.1016/j.jmmm.2017.06.039.
- [9] T. Okamura, R. Rachi, N. Hirano, and S. Nagaya. Refrigeration at room temperature (portoroz). volume 1, page 377, 2007.
- [10] Botoc, D., Siroux, M., and Salceanu, A. Magnetic refrigeration: emerging technology for sustainable refrigeration. *E3S Web Conf.*, 294:03001, 2021. doi: 10.1051/e3sconf/202129403001.
- [11] Z. Bontinck, J. Corno, H. De Gersem, S. Kurz, A. Pels, S. Schöps, F. Wolf, C. Falco, J. Dölz, R. Vázquez, and U. Römer. Recent advances of isogeometric analysis in computational electromagnetics. *International Computing Society*, 09 2017. doi: 10.48550/arXiv.1709.06004.

- [12] L. Piegl and W. Tiller. *The NURBS Book*. Springer, 2 edition, 1997.
- [13] J. D. Jackson. *Classical Electrodynamics*. Wiley & Sons, 3rd edition. ISBN 978-0-471-30932-1. doi: 10.1017/CBO9780511760396.
- [14] S. Salon. *Finite Element Analysis of Electrical Machines*. Kluwer, 1995.
- [15] A. Kitanovski. Energy applications of magnetocaloric materials. *Advanced Energy Materials*, 10(10):1903741, 2020. doi: 10.1002/aenm.201903741.
- [16] M. Merkel, P. Gangl, and S. Schöps. Shape optimization of rotating electric machines using isogeometric analysis. *IEEE Transactions on Energy Conversion*, 36(4):2683–2690, 2021. doi: 10.1109/TEC.2021.3061271.
- [17] C. Ding, X. Cui, G. Huang, G. Li, K. Tamma, and Y. Cai. A gradient-based shape optimization scheme via isogeometric exact reanalysis. *Engineering Computations*, 35, 10 2018. doi: 10.1108/EC-08-2017-0292.
- [18] Z. Bontinck, Jacopo Corno, Sebastian Schöps, and Herbert De Gersem. Isogeometric analysis and harmonic stator-rotor coupling for simulating electric machines. *Computer Methods in Applied Mechanics and Engineering*, 334:40–55, 2018. ISSN 0045-7825. doi: 10.1016/j.cma.2018.01.047.
- [19] H. Egger, M. Harutyunyan, R. Löscher, M. Merkel, and S. Schöps. On torque computation in electric machine simulation by harmonic mortar methods. *Journal of Mathematics in Industry*, 12(1), 1 2022. doi: 10.1186/s13362-022-00121-2.
- [20] H. Egger, M. Harutyunyan, M. Merkel, and S. Schöps. On the stability of harmonic coupling methods with application to electric machines. In *Scientific Computing in Electrical Engineering*, pages 117–125. Springer International Publishing, 2021.
- [21] L. Harzheim. *Strukturoptimierung: Grundlagen und Anwendungen*. 2008. ISBN 9783808556580.
- [22] R. Bjørk, C. Bahl, and A. Insinga. Topology optimized permanent magnet systems. *Journal of Magnetism and Magnetic Materials*, 437, 04 2017. doi: 10.1016/j.jmmm.2017.04.028.
- [23] K. Engelbrecht, D. Eriksen, C.R.H. Bahl, R. Bjørk, J. Geyti, J.A. Lozano, K.K. Nielsen, F. Saxild, A. Smith, and N. Pryds. Experimental results for a novel rotary active magnetic regenerator. *International Journal of Refrigeration*, 35(6):1498–1505, 2012. ISSN 0140-7007. doi: 10.1016/j.ijrefrig.2012.05.003.
- [24] J. M. D. Coey. *Magnetism and Magnetic Materials*. Cambridge University Press, 2010. doi: 10.1017/CBO9780511845000.
- [25] O. Sigmund and K. Maute. Topology optimization approaches. *Structural and Multidisciplinary Optimization*, 48(6):1031–1055, December 2013. ISSN 1615-1488. doi: 10.1007/s00158-013-0978-6.
- [26] Penguian. Nurbs toolbox by d.m. spink. URL <https://www.mathworks.com/matlabcentral/fileexchange/26390-nurbs-toolbox-by-d-m-spink>.
- [27] B. Bader and T. Kolda. Tensor toolbox for matlab, version 3.2.1, 2021. URL <https://www.tensortoolbox.org/>.
- [28] C. de Falco, A. Reali, and R. Vázquez. GeoPDEs: A research tool for isogeometric analysis of PDEs. *Advances in Engineering Software*, 42 (12):1020–1034, 2011.
- [29] R. Vázquez. A new design for the implementation of isogeometric analysis in Octave and Matlab: GeoPDEs 3.0. *Computers and Mathematics with Applications*, 2016. To appear.
- [30] Matlab. Optimization toolbox, 2022. URL <https://de.mathworks.com/products/optimization.html>.
- [31] D. Dimitrov, K. Fikiin, and R. Kirilov. Potential of magnetocaloric refrigeration for cold chain applications. 05 2006. doi: 10.13140/RG.2.2.16199.01441.
- [32] T. Kanluang, Y. Hanlumuang, and R. Techapiesanchaorenkij. Design and development of magnetic refrigeration prototype for the performance analysis of magnetocaloric materials. *Journal of Physics Conference Series*, 2018. doi: 10.1088/1742-6596/1144/1/012065.
- [33] Y. You, Y. Guo, S. Xiao, S. Yu, H. Ji, and X. Luo. Numerical simulation and performance improvement of a multi-polar concentric halfbach cylindrical magnet for magnetic refrigeration. *Journal of Magnetism and Magnetic Materials*, 405:231–237, 2016. ISSN 0304-8853. doi: 10.1016/j.jmmm.2015.12.077.
- [34] A. Insinga. *Optimising Magnetostatic Assemblies*. PhD thesis, Technical University of Denmark, 2016. Department of Energy Conversion and Storage.
- [35] A. R. Insinga, R. Bjørk, and A. Smith. Optimally segmented permanent magnet structures. *IEEE Transactions on Magnetics*, 52(12), 2016. doi: 10.1109/TMAG.2016.2593685.
- [36] D. Benke, Maximilian Fries, Tino Gottschall, Dominik Ohmer, Andreas Taubel, Konstantin Skokov, and Oliver Gutfleisch. Maximum performance of an active magnetic regenerator. *Applied Physics Letter*, 2021. doi: <https://doi.org/10.1063/5.0067751>.
- [37] D. Benke, M. Fries, M. Specht, J. Wortmann, M. Pabst, T. Gottschall, I. Radulov, K. Skokov, Alex I. Bevan, D. Prosperi, C. O. Tudor, P. Afiuny, M. Zakotnik, and O. Gutfleisch. Magnetic refrigeration with recycled permanent magnets and free rare-earth magnetocaloric la–fe–si. *Energy Technology*, 8(7):1901025, 2020. doi: 10.1002/ente.201901025.
- [38] J. Chaudron, C. Muller, M. Risser, and S. Lionte. Performance measurements on a large-scale magnetocaloric cooling application at room temperature. 09 2018. doi: 10.18462/iir.thermag.2018.0022.
- [39] R. Gozdur, P. Gebara, and K. Chwastek. A study of temperature-dependent hysteresis curves for a magnetocaloric composite based on La(Fe, Mn, Si)13-H type alloys. *Energies*, 13(6), 2020. doi: 10.3390/en13061491.
- [40] M. Krautz, M. Beyer, C. Jäschke, L. Schinke, A. Waske, and J. Seifert. A magnetocaloric booster unit for energy-efficient air-conditioning. *Crystals*, 9(2), 2019. ISSN 2073-4352. doi: 10.3390/cryst9020076.
- [41] H. R. E. H. Bouchekara, A. Kedous-Lebouc, and J. P. Yonnet. Electromagnetic Design of a Magnetic Field Source for a Magnetocaloric Refrigerator. *Progress In Electromagnetics Research*, 19:251–263, 2011. doi: 10.2528/PIERM11062708.
- [42] J. A. Lozano, M. S. Capovilla, P. V. Trevizoli, K. Engelbrecht, C. R. H. Bahl, and J. R. Barbosa. Development of a novel rotary magnetic refrigerator. *International Journal of Refrigeration*, 68:187–197, 2016. ISSN 0140-7007. doi: 10.1016/j.ijrefrig.2016.04.005.
- [43] P. Trevizoli, Alan T. Nakashima, Guilherme F. Peixer, and Jader R. Barbosa. Performance assessment of different porous matrix geometries for active magnetic regenerators. *Applied Energy*, 187:847–861, 2017. ISSN 0306-2619. doi: 10.1016/j.apenergy.2016.11.031.
- [44] J. Tušek, A. Kitanovski, S. Zupan, I. Prebil, and A. Poredoš. A comprehensive experimental analysis of gadolinium active magnetic regenerators. *Applied Thermal Engineering*, 53(1):57–66, 2013. ISSN 1359-4311. doi: 10.1016/j.applthermaleng.2013.01.015.